



Origin of negative thermal expansion and pressure-induced amorphization in zirconium tungstate from a machine-learning potential

Ri He ¹, Hongyu Wu,¹ Yi Lu,^{2,3} and Zhicheng Zhong ^{1,4,*}

¹Key Laboratory of Magnetic Materials Devices & Zhejiang Province Key Laboratory of Magnetic Materials and Application Technology, Ningbo Institute of Materials Technology and Engineering, Chinese Academy of Sciences, Ningbo 315201, China

²National Laboratory of Solid State Microstructures and Department of Physics, Nanjing University, Nanjing 210093, China

³Collaborative Innovation Center of Advanced Microstructures, Nanjing University, Nanjing 210093, China

⁴China Center of Materials Science and Optoelectronics Engineering, University of Chinese Academy of Sciences, Beijing 100049, China



(Received 25 July 2022; revised 2 October 2022; accepted 25 October 2022; published 4 November 2022)

Understanding various macroscopic pressure-volume-temperature properties of materials on the atomistic level has always been an ambition for physicists and material scientists. Particularly, some materials such as zirconium tungstate (ZrW_2O_8), exhibit multiple exotic properties including negative thermal expansion (NTE) and pressure-induced amorphization (PIA). Here, using machine-learning based deep potential, we trace both of the phenomena in ZrW_2O_8 back to a common atomistic origin, where the nonbridging O atoms play a critical role. We demonstrate that the nonbridging O atoms confer great flexibility to vibration of polyhedra, and kinetically drive volume shrinking on heating, or NTE. In addition, beyond a certain critical pressure, we find that the migration of nonbridging O atoms leads to additional bond formation that lowers the potential energy, suggesting that the PIA is a potential-driven first-order phase transition. Most importantly, we identify a second critical pressure beyond which the amorphous phase of ZrW_2O_8 undergoes a “hidden” phase transition from a reversible phase to an irreversible one.

DOI: [10.1103/PhysRevB.106.174101](https://doi.org/10.1103/PhysRevB.106.174101)

I. INTRODUCTION

Macroscopic properties of materials are deeply rooted in their underlying atomic arrangement and interaction, and understanding these properties on an atomistic level has been a long-sought endeavor [1]. Temperature and external pressure, two of the most commonly used “tuning knobs” for manipulating physical properties of materials to date, have led to the discovery of numerous exotic phenomena such as negative thermal expansion (NTE) [2–4], liquid-liquid second critical point [5–7], and pressure-induced high-temperature superconductivity [8,9]. Establishing a clear relationship between these macroscopic properties and the atomistic behavior is not only important from a fundamental perspective, but also holds the key for rational material design. It yet remains a highly nontrivial task due to the large number of degrees of freedom inherent to a macroscopic system, which are usually difficult to capture in microscopic theories.

Take the NTE for example, which refers to the counterintuitive phenomenon that certain materials contract upon heating [3,4]. NTE materials are relatively rare and ZrW_2O_8 is one of the most representative ones among them. ZrW_2O_8 exhibits volume reduction with increasing temperature from 0.3 to 1050 K [10]. The nature of the local mechanism responsible for its NTE remains controversial as the exact atomic structure details on heating can only be indirectly inferred from experiment with certain model assumption [11–13]. One of

the most common explanations is the rigid-unit modes (RUM) model, in which the transverse vibrations of O atoms can only occur through coupled liberations of tetrahedra and octahedra forming the structure [14–17], although its validity needs to be verified by microscopic calculations that have so far remained elusive.

In addition to NTE, ZrW_2O_8 exhibits another interesting property, namely the pressure-induced amorphization transition (PIA). Perottoni *et al.* showed that above 1.5 GPa, crystalline ZrW_2O_8 transforms to an amorphous phase that persists after pressure release at ambient conditions [2,18,19]. While some theoretical research suggests that the PIA and NTE may have a common origin [20], the exact mechanism of PIA in ZrW_2O_8 is still heavily debated [21–25], as the complexity of disordered atomic structure poses serious challenges to traditional theoretical methods such as the classical atomic force field, which describes bonded and nonbonded interactions in solids using some prescribed functions with fitted parameters that severely limit the flexibility of the force fields [13,14]. The lack of periodicity, and consequently a small enough unit cell, in amorphous materials also prevents its accurate description using methods such as density-functional theory (DFT), whose computation complexity scales polynomially with the unit-cell size.

To solve this outstanding problem and determine the atomistic origin of the NTE and PIA, in this study we develop a machine-learning (ML)-based deep potential (DP) for ZrW_2O_8 using training data from DFT calculations. ML-based potentials have the flexibility and nonlinearity necessary to describe complex ordered and disordered interatomic

*zhong@nimte.ac.cn

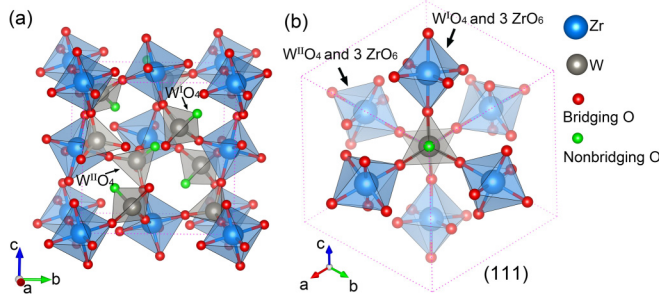


FIG. 1. Structure of cubic ZrW_2O_8 unit cell. (a) cubic cell consists of a network of corner-shared octahedral ZrO_6 and tetrahedral WO_4 . The octahedral ZrO_6 are equivalent but the tetrahedral WO_4 can be divided into $\text{W}^{\text{I}}\text{O}_4$ and $\text{W}^{\text{II}}\text{O}_4$ depending on the length of nonbridging W–O bond. (b) (111) direction view of cubic cell.

environment from the perspective of “many body” using a deep neural network [26,27]. Therefore, the DP method is first principle without any empirical parameter [13,28]. While still in infancy state, they have been successfully applied to the investigation of various processes in complex material systems [29], including phase transition [30–32], nucleation [33], chemical catalysis [34], gas combustion [35], and atomic layer deposition of film growth [36].

Herein, we find that the well-trained DP can describe the structure and other structure-related properties of ZrW_2O_8 over a wide temperature and pressure range. Using the DP, the calculated NTE and PIA in ZrW_2O_8 show great agreement with experimental results. Importantly, DP-calculated results reveal that the NTE and PIA originate from a common factor, namely the nonbridging O atoms. For NTE, the nonbridging O confers great flexibility to the rotation of tetrahedra and octahedra that lead to volume contraction upon heating. In addition, the nonbridging O atoms move into a neighboring polyhedron above a critical pressure of 1.4 GPa and form additional bonds to lower the thermodynamical potential energy, driving a first-order amorphization phase transition as observed in experiments. Furthermore, we predict that further increasing the pressure to a second critical value of 3.8 GPa induces a hidden phase transition from an a^{I} reversible phase to an a^{II} irreversible one. Our paper paves the path for further investigation on the dynamics of other NTE materials like the flexible framework cyanides [28], Coulomb floppy networks empty perovskites fluorides [37], as well as recently proposed two-dimensional NTE materials like tetragonal oxalate-based metal-organic framework $\text{CdZrSr}(\text{C}_2\text{O}_4)_4$ [38], graphitelike LiBO_2 layers [39], and CrBr_3 [40], which are not subject to RUM-based NTE mechanisms. We expect the current ML-based DP model can be improved and extended, enabling large-scale atomistic simulations of the doping effect and other related exotic behaviors in NTE materials.

II. RESULTS

A. Accurate deep-learning potential

The crystal structure of ZrW_2O_8 at 0 to 430 K is cubic phase with $P2_13$ space group as illustrated in Fig. 1. The unit cell consists of a network of corner-shared octahedral ZrO_6 and tetrahedral WO_4 . The six octahedral ZrO_6 are equivalent

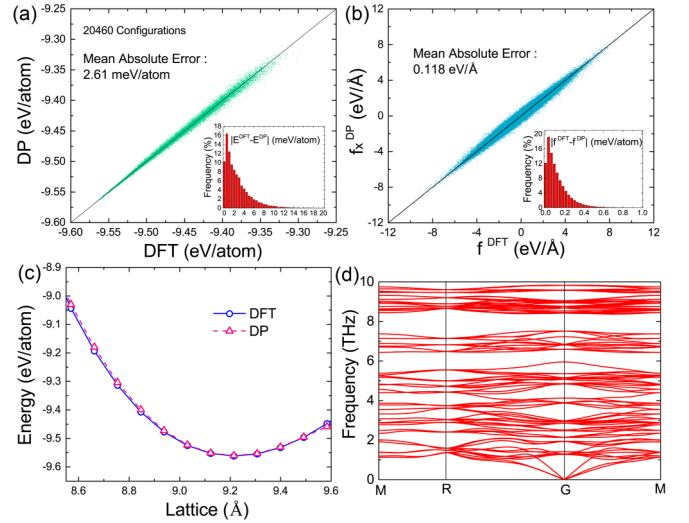


FIG. 2. Benchmark test of DP against DFT results. Comparison of energies (a) and atomic forces (b) calculated using the DP and DFT for all configurations. DP and DFT energies for different hydrostatic pressure (c) and phonon dispersion relations (d) for cubic phase.

and each share all their six corners with neighboring WO_4 tetrahedra, while the eight tetrahedral WO_4 each share only three of their four O atoms with the neighboring octahedral ZrO_6 , leaving one W–O bond dangling. We refer to the corresponding O atom as the nonbridging O (marked by green spheres in Fig. 1). The tetrahedral WO_4 can be divided into two types depending on the length of nonbridging W–O bond. The WO_4 tetrahedra with shorter (longer) W–O bond are labeled as $\text{W}^{\text{I}}\text{O}_4$ ($\text{W}^{\text{II}}\text{O}_4$). All the crystalline phase-related results in the main text are based on the cubic α - ZrW_2O_8 , while the discussion of β phase and γ phase can be found in Supplemental Material [41]. The DFT optimized ground-state cubic phase is used as the initial structure to explore all the characteristic configurations of high-temperature crystal and high-pressure amorphous. The 20 460 configurations with different temperatures and pressures used in the training dataset are explored by the DP-GEN concurrent learning procedure [42], and the deep neural network-based DP is trained using the DeePMD method (for details, see Methods) [26,27].

Once the well-trained deep neural-network based DP is obtained, it is first benchmarked against DFT results to access its accuracy. We compare the energies and atomic forces calculated using the DP and DFT for 20 460 configurations in the final training dataset. We find a good agreement between DP- and DFT-calculated energies and forces with a mean absolute error are 2.61 meV per atoms and 0.12 eV/Å, respectively, as shown in Figs. 2(a) and 2(b). In comparison, the classical force field of ZrW_2O_8 proposed by Pryde *et al.* [14] vastly overestimates atomic forces due to the limitations imposed by the preset functions and fitted parameters (Fig. S1), and fails to predict atomic interactions involving the bond formation and -breaking under pressure [43]. The equations of state of cubic phase calculated by DFT and DP are presented in Fig. 2(c). The DP model reproduces well the DFT energy profile over a wide range of lattice constants from 8.5 to 9.6 Å. The equilibrium lattice constants opti-

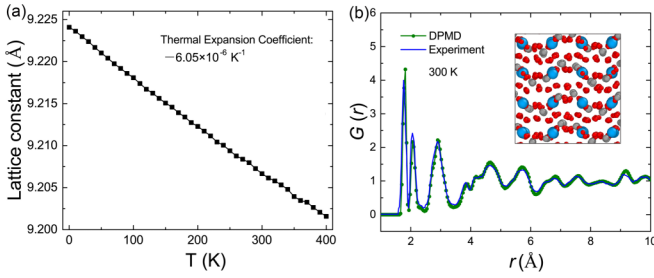


FIG. 3. Crystal structural properties of ZrW_2O_8 on heating. (a) Variation of cubic ZrW_2O_8 lattice parameter with temperature from DPMD at ambient pressure. (b) Neutron-weighted pair-distribution functions $G(r)$ from cubic ZrW_2O_8 at 300 K and 1 bar calculated from DPMD and experiment.

mized by DFT and DP for cubic phase are 9.215 and 9.223 Å, respectively. We also use the DP to calculate the elastic constants for cubic phases and compare the values with DFT results. The results are shown in Table SI, again demonstrating great agreement between DP and DFT. Phonon dispersion spectrum is the quantum-mechanical description of an atomic vibrational motion along different wave vectors, where the atomic force plays an important role. Accurate calculation of phonon dispersion is a strict criterion for testing the accuracy of DP. The calculated phonon dispersion of the cubic ZrW_2O_8 by the DP is shown in Fig. 2(d). The 44-atom unit cell produces 3 acoustic and 129 optical branches. The three acoustic branches exist only in the low-frequency regime, and approach zero frequency towards the high-symmetry Gamma point. No negative phonon frequencies in the phonon dispersion indicates the dynamical stability of ZrW_2O_8 at room temperature and ambient pressure, which agrees well with the DFT results [44]. The systematic benchmark shows that the DP has excellent DFT-level accuracy, and is capable of predicting a range of temperature and pressure properties of ZrW_2O_8 from first principles.

B. Origin of negative thermal expansion

Once the DFT-level accuracy of DP is confirmed, we can use it to investigate the evolution of crystal structural properties of ZrW_2O_8 on heating by deep-potential molecular-dynamics (DPMD) simulations using a much larger system. Figure 3(a) shows the lattice constant variation of a 7.3-nm \times 7.3-nm \times 7.3-nm supercell (including 22 528 atoms) with increasing temperature at ambient pressure. It can be clearly seen that the lattice constant exhibits a continuous shrink from 0 to 1000 K (also see Supplemental Material, Fig. S2 [41]). This result demonstrates an excellent isotropic NTE property of ZrW_2O_8 . The DP-calculated coefficient of thermal expansion is $-6.2 \times 10^{-6} \text{ K}^{-1}$, in good agreement with reported experimental results of -4×10^{-6} to $-9 \times 10^{-6} \text{ K}^{-1}$ [10,45]. The neutron pair-distribution functions $G(r)$ at room temperature obtained with the DPMD simulations are shown in Fig. 3(b). The excellent agreement between the calculation and the experimental result [23] confirms that the DP can well capture the atomic structural characteristics of ZrW_2O_8 at room temperature.

Many early works have aimed at identifying the mechanism for NTE. Despite that it is commonly believed that the NTE relies on the so-called tension effect and atomic structure specifics in a floppy network material [17,28,46,47], the exact origin of NTE in ZrW_2O_8 is still controversial and has been attributed to a variety of mechanisms. For instance, the “RUM” model suggests that the transverse vibrations of the O atoms in the middle of W-O-Zr linkage are the result of whole-body rotations and translations of the linked octahedral ZrO_6 and tetrahedral WO_4 with essentially no distortion, pulling the Zr and W atoms closer and thus causing the NTE (a sketch is shown in Fig. S3) [10,14–16]. In contrast, the “Tent” model assumes a stiff W-O-Zr linkage, and NTE derives from the translational motion of tetrahedral WO_4 along the (111) direction and the correlated motion of the three nearest octahedral ZrO_6 [11,12]. In other words, the main controversy between the RUM and Tent models lies in the relative stiffness of the W-O-Zr linkage.

To resolve the above controversy, we investigate the thermal expansion of neighboring atom pair distances (or bond length) and the degree of rigidity of corner-sharing polyhedra. In DPMD simulations, each atom at \mathbf{r}_i vibrates about its mean position $\langle \mathbf{r}_i \rangle$. The atomic distances between two atoms can thus take an “apparent” value $\mathbf{R} = |\langle \mathbf{r}_i \rangle - \langle \mathbf{r}_j \rangle|$, which is the difference between their mean positions, and a time-dependent “true” value $\mathbf{r} = |\mathbf{r}_i - \mathbf{r}_j|$ [3,13]. The former defines the lattice constants and can be directly determined by x-ray- or neutron-diffraction measurements. The latter contains more detailed dynamical properties of the lattice but is not easily probed in experiments. A similar consideration can be used to define apparent and true angles of W-O-Zr linkage. The DPMD results obtained for apparent and true bond length (atom pair distance) of W-O, Zr-O, Zr-W, Zr-Zr, and angle of Zr-O-W at different temperatures are presented in Fig. 4 (for $\text{W}^{\text{I}}\text{O}_4$ and three nearest ZrO_6) and Fig. S4 (for $\text{W}^{\text{II}}\text{O}_4$ and three nearest ZrO_6). It clearly indicates that the W-O (Zr-O) bonds display a negative thermal expansion coefficient of $-1.542 \times 10^{-5} \text{ K}^{-1}$ ($-0.377 \times 10^{-5} \text{ K}^{-1}$) for the apparent bond length, but a positive one of 0.504 K^{-1} ($1.548 \times 10^{-5} \text{ K}^{-1}$) for the true bond length. The DPMD results reveal that the asymmetry of atomic interaction potential causes an increase in the mean instantaneous distance between the bonded atoms as the temperature increases, but the distance between the mean positions of two atoms tends to decrease. These results show that both the RUM and Tent models are only partially right. On one hand, the observed expansion of the WO_4 tetrahedra and ZrO_6 octahedra invalidates the rigid-polyhedron assumption in the RUM model. On the other hand, while the apparent W-O-Zr angle Φ remains nearly constant at $\sim 155.5^\circ$, in a seeming agreement with the assumption of the Tent mode, the true W-O-Zr angle $\langle \varphi \rangle$ decreases drastically with increasing temperature as shown in Fig. 4(c). In reality, the expansion of true W-O and Zr-O bonds is overcompensated by the decrease of the true W-O-Zr angle caused by the transverse vibrations of the O atom in the middle of the Zr-O-W linkage [Fig. 4(f)], and their combined effect results in the observed NTE, as reflected in the reduction of the overall lattice constants as well as the Zr-W and Zr-Zr distances [Figs. 4(d) and 4(e) and Supplemental Material, Fig. S5 [41]]. Similar RUM results were reached in zinc cyanide, where

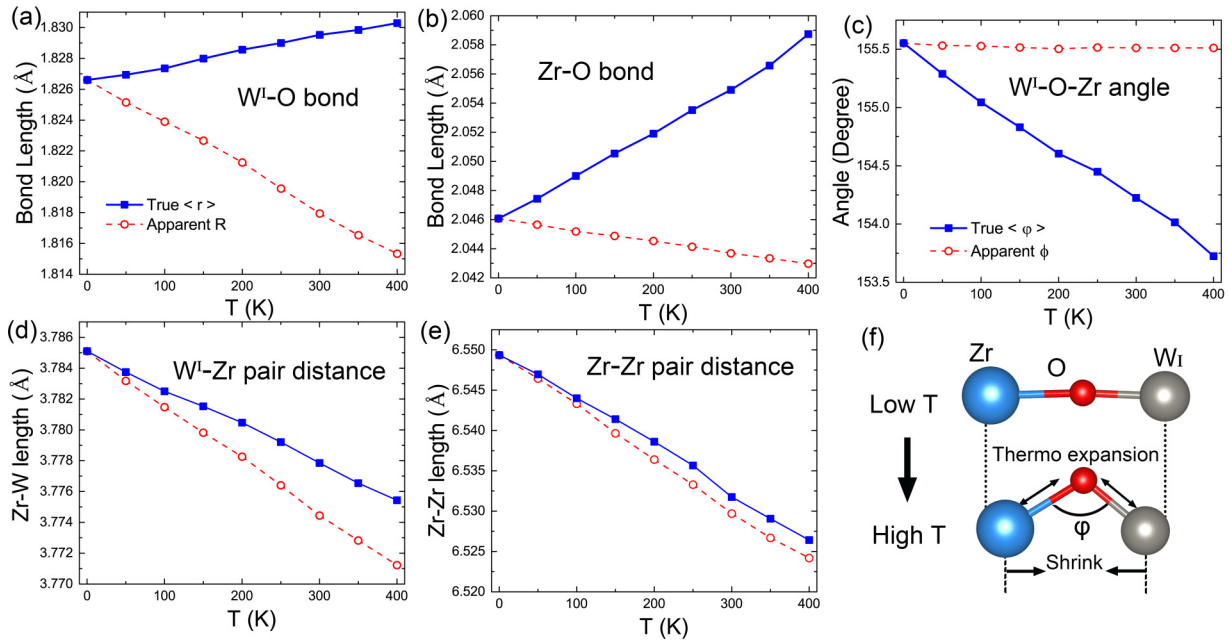


FIG. 4. Thermal expansion of neighboring atom-pair distances and degree of corner-sharing polyhedra. “True” and “apparent” bond length/atom pair of (a) W-O, (b) Zr-O, (d) Zr-W, (e) Zr-Zr, and angle of (c) Zr-O-W as a function of temperature. (f) Sketch of bond length and angle variation on heating.

the rotations of neighboring tetrahedra accompanied by lateral translations of the tetrahedra was observed in MD simulations [28,46]. Significant rotations of the ScF_6 octahedra were also revealed in Coulomb floppy networks empty perovskites scandium trifluoride by effective Hamiltonian model [47].

C. Pressure-induced amorphous phase and its reversibility

The amorphization transition under high pressure is another key feature of ZrW_2O_8 . While the NTE and the PIA are believed to be closely linked [18,23,48], the detailed complex atomic structure of amorphous ZrW_2O_8 has been a subject of debate. To resolve this issue, we further perform DPMD simulations of ZrW_2O_8 under different pressure (0.2 ~ 4.4 GPa) at 300 K for 50 ps, with subsequent pressure relaxation to

1 bar for 100 ps. The structural properties as a function of time are shown in Fig. 5(a), and the lattice constant dependence on pressure for compression (red line) and decompression (blue line) processes are shown in Fig. 5(b). Upon application of pressure, it can be observed that the lattice constant decreases slightly by 0.05 Å from 1 bar to 1.3 GPa. Analysis of structural partial radial distribution functions (RDFs), obtained from DPMD simulations, can offer a detailed description of the observed structural phase transition from crystal to amorphous on an atomistic level. In the pressure range between 1 bar and 1.3 GPa, the partial O-O RDFs in Fig. 6(a) clearly show that the ZrW_2O_8 maintains perfect crystalline structure. The corresponding atomic structures of crystalline phase are shown in Supplemental Material, Figs. S6(a)–S6(c) [41]. The crystalline ZrW_2O_8 under pressure still exhibits excellent NTE

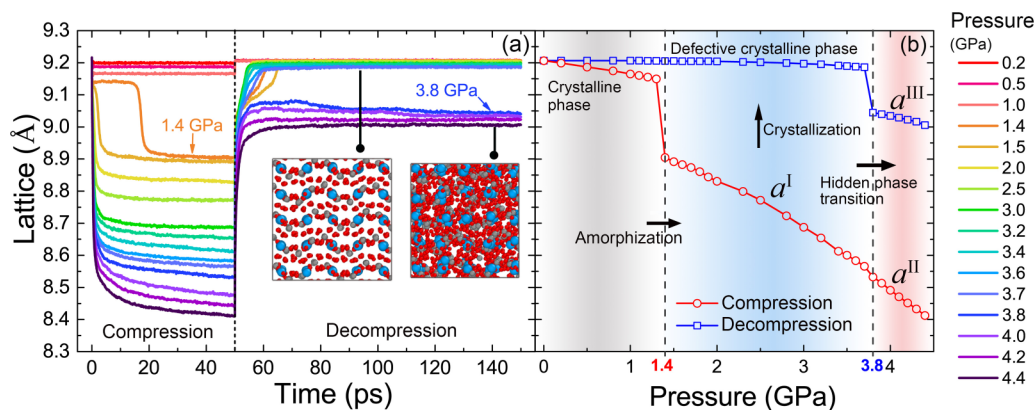


FIG. 5. Structural properties of ZrW_2O_8 with compression and decompression. (a) Variation of lattice parameter with time on compression from 0.2 to 4.4 GPa at 300 K and then upon decompression. (b) Lattice parameter depends on pressure for compression after 50 ps (red line) and decompression after 100 ps (blue line).

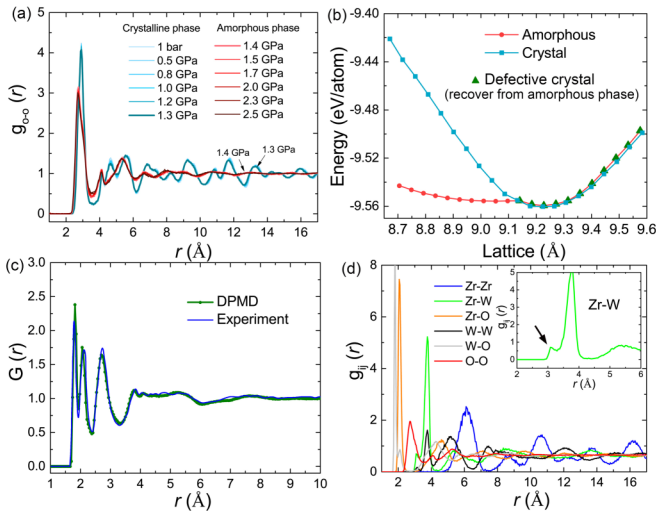


FIG. 6. Analysis of the atomic structure and potential energy of ZrW_2O_8 at different pressures. (a) Partial O-O RDFs, $g_{\text{O-O}}(r)$, of ZrW_2O_8 at different pressures from DPMD simulations at 300 K. (b) Energy variations of cubic and amorphous phase ZrW_2O_8 with hydrostatic pressure (lattice parameter variation), and amorphous is energy favored for the lattice constant smaller than ~ 9.13 Å. (c) Neutron-weighted pair-distribution functions $G(r)$ and (d) radial distribution function $g_{ij}(r)$ of amorphous ZrW_2O_8 at 3 GPa calculated from DP model and experiment.

property (see Supplemental Material, Fig. S7 [41]). Increasing the pressure beyond 1.4 GPa, the O-O RDF peaks vanish at distances larger than 8 Å [see Fig. 6(a)]. This substantial modification indicates that ZrW_2O_8 undergoes an amorphization transition. The snapshots of corresponding atomic structures for 1 bar to 2.5 GPa in Supplemental Material, Fig. S6 also clearly show that a disordered structure forms above 1.4 GPa [41]. Accompanying the PIA is a sudden decrease of lattice constant from 9.16 to 8.89 Å [Fig. 5(b)], which shows the first-order nature of the phase transition. The amorphous ZrW_2O_8 does not exhibit NTE properties as shown in Supplemental Material, Fig. S7 [41]. The calculated PIA critical pressure 1.4 GPa is well comparable to the experimental value of 1.5 GPa [2]. In Fig. 5(b), it is observed that the pressure-induced softening, i.e., elastic moduli become softer under compression, in both the crystalline and the amorphous phases. The DP-calculated pressure-induced softening is in good agreement with the experimental observation [25]. Indeed, most NTE materials with framework structures will show pressure-induced softening such as silica [49], zinc cyanide [50], and scandium trifluoride [37]. Fang *et al.* have demonstrated that the pressure-induced softening and NTE are closely linked because both the pressure and the heating thermal fluctuations will cause instantaneous buckling of the atomic linkages [51–53]. Interestingly, the amorphous ZrW_2O_8 also exhibits pressure-induced softening although it does not exhibit NTE properties (Fig. S7) [41]. The possible pressure-induced softening in amorphous phase is an unexpected result. The origin of the pressure-induced softening in amorphous phase may involve complicated cooperative atomic interplay. One possible origin might be the diffusion of O atoms, as it induces volume shrinking of the amorphous phase. Future studies

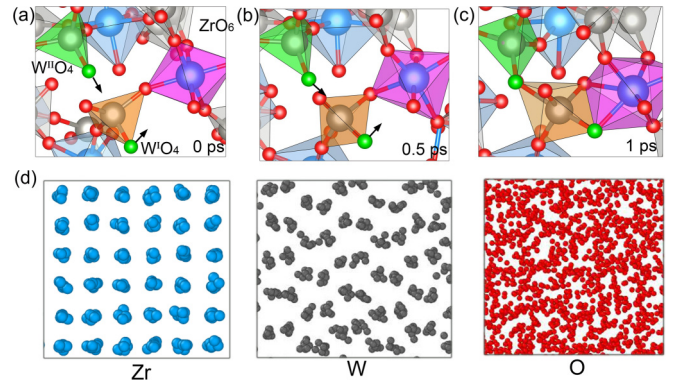


FIG. 7. Atomic structure evolution of amorphous ZrW_2O_8 at 3 GPa. (a)–(c) Movement of nonbridging O (marked in green) result in formation of ZrO_7 decahedron and WO_5 octahedron. (d) Partial snapshot of amorphous 22 528-atom supercell; the arrangements of Zr, W, and O are presented, respectively.

are required to further pin down the exact nature of this effect.

To reveal the exact origin of PIA in ZrW_2O_8 , we explore the energy stability of cubic and amorphous phases as a function of hydrostatic pressure (i.e., lattice isotropic variation) by DP atomic relaxation at absolute zero, which will eliminate the contribution of kinetic energy induced by thermal perturbation. We emphasize that such calculations for amorphous phase are far beyond the capacity of DFT because of calculating spatial scale limitation. In the calculations, the amorphous phase can be stabilized strain-free with the optimized lattice constant 9.005 Å, much smaller than the 9.224 Å for cubic phase, and the corresponding atomic structures are shown in Supplemental Material, Fig. S8(a) and S8(b) [41]. The resulting energy-versus-lattice diagram is shown in Fig. 6(b). It shows that the amorphous phase is energetically favored for lattice constant smaller than ~ 9.13 Å. As lattice constant is increased, the amorphous phase rapidly becomes unstable and transitions to a “defective” crystalline structure, where a small number of O atoms could not return to its perfect lattice site, forming edge-shared polyhedral defects in cubic phases as shown in Fig. S8(c) (it will be explained in detail below) [41]. The energy of these defective cubic phases is very close to that of perfect cubic phase, as shown by green triangles in Fig. 6(b). Our results show that the driving force of PIA in ZrW_2O_8 is the potential energy.

We proceed to analyze the detailed local structure of the amorphous phase. The DP-calculated neutron-weighted pair-distribution functions $G(r)$ and partial RDF $g_{ij}(r)$ of the amorphous phase at 300 K and at 3 GPa are shown in Figs. 6(c) and 6(d). The calculated $G(r)$ is almost on top of the experimental data [23]. We analyze the dynamic behavior of atoms during the amorphization transition under pressure. The local dynamic processes are shown in Figs. 7(a)–7(c). As mentioned above, ZrW_2O_8 crystallizes in cubic phase with the networks of corner-linked octahedral ZrO_6 and tetrahedral WO_4 , which is highly flexible. As the high pressure (above 1.4 GPa) is applied, the one nonbridging O in $\text{W}^{\text{I}}\text{O}_4$ [green spheres in Fig. 7(a)] moves into a neighboring octahedral ZrO_6 , and another one in $\text{W}^{\text{II}}\text{O}_4$ moves to a neighboring

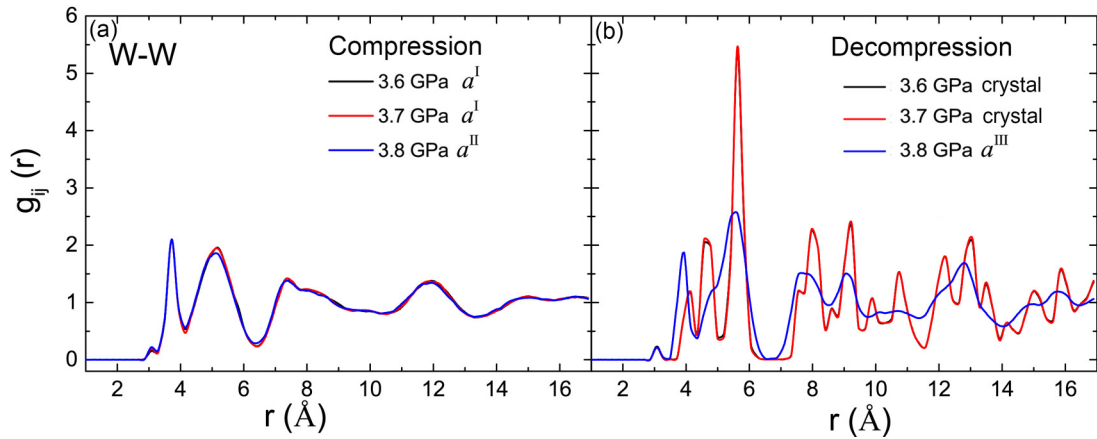


FIG. 8. Partial W-W RDFs of ZrW₂O₈ at different pressures. (a) RDFs at different pressure and (b) RDFs upon decompression.

tetrahedral W^IO₄ [Fig. 7(b)], forming an edge-shared decahedral ZrO₇ and pentahedral W^IO₆ structure as shown in Fig. 7(c). This edge-shared structure produces the first peak in 3.14 Å of partial RDF of Zr-W [marked by arrows in inset of Fig. 6(d)]. The weakness of that peak intensity indicates that the above dynamic behavior happens randomly throughout the system. The equilibrated snapshot of the supercell after amorphization at 3 GPa is shown in Supplemental Material, Fig. S9 [41], several unique configurations of corner-shared and edge-shared polyhedra were formed by movement of nonbridging O atoms. Examination of the species-specific structure in Fig. 7(d) [with the corresponding RDFs in Fig. 6(d)] reveals an interesting aspect of the amorphous phase: the amorphous-like O sit within an almost periodic crystal-like Zr and W coordination array. We note that this structure is in consistent with the proposed reverse Monte Carlo model of amorphous ZrW₂O₈ fitting from experiment data [23].

We next consider the reversibility of the amorphous phase upon decompression. Experiments have confirmed that the PIA in ZrW₂O₈ is irreversible at room temperature, and recrystallization only occurs when heated above 900 K [2,48]. In this study, the subsequent DPMD simulations were performed for decompressions from various pressures (0.2 ~ 4.4 GPa) to ambient conditions. The decompression structural property and RDFs results are shown in Fig. 5 (the atomic structures are shown in Supplemental Material, Fig. S10) and Fig. 8 (also see Supplemental Material, Fig. S11) [41], and it indicates that pressure-induced amorphous phase can be divided into two categories: (i) For the amorphous phase with 1.4 to 3.7 GPa, significant modifications in the RDF of W-W are observed upon decompression. The second peak at 4.1 Å becomes weaker while a new peak at slightly longer distance, 4.4 Å, appears, which indicates it can recover to crystalline phase after pressure release, so we defined it as the a^I reversible phase. (ii) For the amorphous with pressure above 3.8 GPa, the RDF results show that the amorphous phase can be retained upon decompression, which we defined as the a^{II} reversible phase. The same profiles of RDFs of a^I and a^{II} phases in Fig. 8(a) and Supplemental Material, Fig. S11(a) indicate that they have the same equilibrated atomic structure, and they cannot be distinguished by structural characterization in experiment [41]. Therefore, we suggest that amorphous

phase undergoes a hidden phase transition from a^I to a^{II} amorphous phase at the second critical pressure of 3.8 GPa. The RDF of retained a^{III} amorphous is slightly different from the a^I and a^{II} phases, but it exhibits the almost key features of amorphous phase (Fig. 8(b) and Supplemental Material, Fig. S11(b) [41]). The retained a^{III} amorphous phase is quite stable, because it was maintained in subsequent annealing for a long time of 2 ns, as well as at higher temperature of 400 K (Supplemental Material, Fig. S12 [41]). It should be emphasized that the critical pressure of hidden phase transition slightly depends on compression time. For instance, the compression time increases from 50 to 300 ps; the critical pressure decreases from 3.8 to 3.5 GPa (Supplemental Material, Fig. S13 [41]).

For the defective crystalline phase that recovered from a^I phase, the partial W-W RDF is consistent with most of the characteristics of perfect crystalline phase by comparing Supplemental Material, Fig. S11(b) and Fig. S14 [41], except for an additional $g(r)_{W-W}$ peak in the ~3.16 Å [marked by arrows in Fig. 9(a)]. The first additional of $g(r)_{W-W}$ originates from the edge-shared WO₅/WO₆ polyhedra structures in crystalline phase upon decompression. This edge-shared structure can be regarded as a defect in the crystal that formed with compression. By comparing the sliced atomic structure of a^I amorphous phase (3.7 GPa) and recovered crystalline phase in Fig. 9(c), we found that edge-shared WO₅/WO₆ polyhedra are irreversible during crystallization, which is in accord with the RDF result in Fig. 9(a). On the contrary, Fig. 9(b) shows the first peak of $g(r)_{Zr-W}$ disappears in the recovered crystalline phase, which indicates the edge-shared decahedral ZrO₇ and octahedral WO₅ structure recovers to original octahedral ZrO₆ and tetrahedral WO₄ upon decompression [atomic structure evolution is shown in Fig. 9(d)]. The entire sliced atomic structures are shown in Supplemental Material, Fig. S15 [41]. To sum up, the edge-shared WO₅/WO₆ polyhedra are stable and hard to destroy, whereas the edge-shared ZrO₇ and WO₅ polyhedra are relatively unstable.

III. CONCLUSIONS

We have demonstrated that ML-based DP can reach a level of accuracy in the atomic structural modeling of NTE and PIA

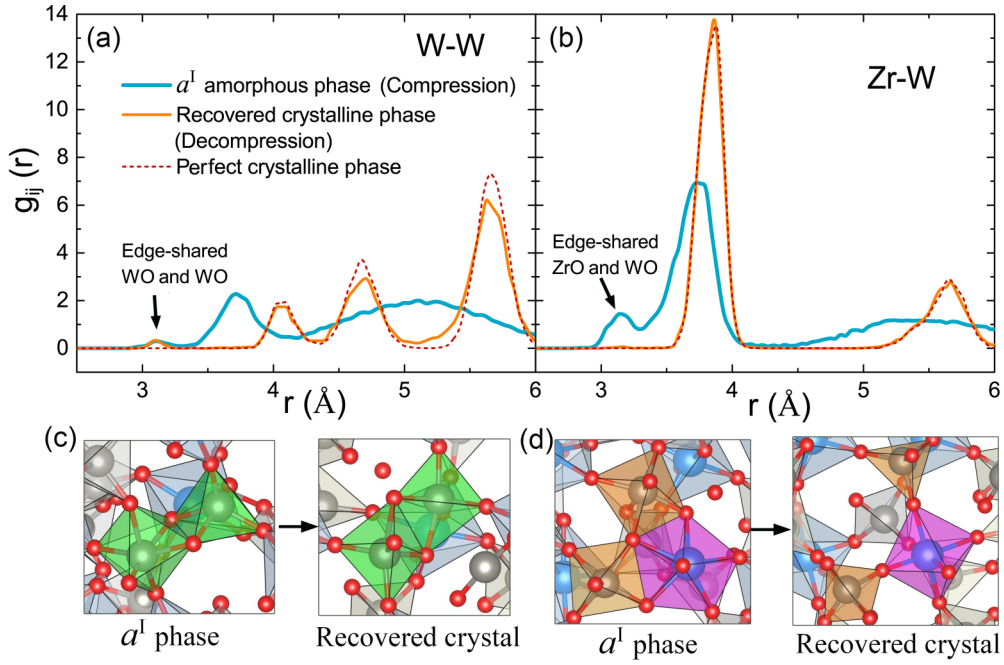


FIG. 9. Analysis of the atomic structure upon decompression. Partial RDFs $g(r)_{ij}$ of pressure-induced a^I amorphous (3.7 GPa) and recovered crystalline phase upon decompression for (a) W-W and (b) Zr-W. The first peak of $g(r)_{W-W}$ and $g(r)_{Zr-W}$ marked in figure corresponding to the edge-shared WO_4/WO_5 and ZrO_7-WO_6 polyhedra. Atomic structural evolution of (c) edge-shared WO_4/WO_5 and (d) ZrO_7-WO_6 polyhedra from a^I phase to recovered crystalline phase.

materials over a wide temperature and pressure range using the example of ZrW_2O_8 . The DP-calculated NTE behavior and coefficient of thermal expansion in ZrW_2O_8 show great agreement with experimental results. By lattice dynamics study of local lattice vibrations, we have shown that both the current RUM and Tent models are only partially reasonable, and the NTE in ZrW_2O_8 originates from the large transverse vibrations of the O atoms in the middle of the Zr-O-W linkage. We further investigated the mechanism of PIA in ZrW_2O_8 . We found that ZrW_2O_8 undergoes a first-order potential-driven amorphization transition above a critical pressure of 1.4 GPa, which is well comparable to experimental value. We also reveal that the migration of O atoms leads to additional bond formation that lowers the potential energy, suggesting that the PIA is a potential-driven transition. Most importantly, we predicted that the amorphous phase undergoes a hidden phase transition from reversible a^I to irreversible a^{II} phase at a second critical pressure of 3.8 GPa, which shall be verified in future experiments. Our study on ZrW_2O_8 not only has important implications for future research on other NTE and PIA materials, but also opens the door for quantitatively accurate atomistic modeling of general materials with direct links to experiments. We believe that the DP method will play a pivotal role in future design of structural and functional materials whose properties depend sensitively on detailed atomic configurations.

IV. METHODS

A. Concurrent learning procedure

Carefully choosing the ZrW_2O_8 configurations used in the training dataset is crucial to the success of training process

and accurate of DP. Because we focus on the NTE and PIA behaviors of ZrW_2O_8 , we need all the characteristic configurations of crystal and amorphous at a wide temperature and pressure range. Most configurations that we need are far from the ground state of cubic phase. In this work, we use the DP Generator (DP-GEN) to generate a set of training data that cover an enough wide range of relevant configurational space efficiently. DP-GEN is a concurrent learning strategy [42], and the workflow of each iteration includes three main steps as illustrated in Fig. 10: (i) Training the deep-learning potentials, (ii) exploration configurations by DPMD simulations, and (iii) labeling configurations according to certain criteria and added into training dataset.

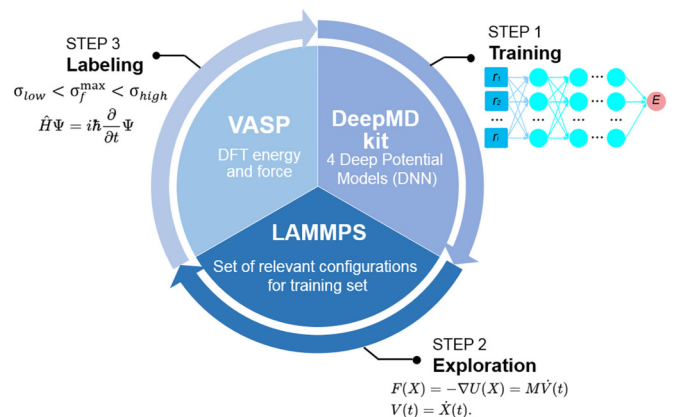


FIG. 10. Deep-learning potential training procedure, including training, exploration, and labeling.

We start with DFT-optimized ground-state structures of $P2_13$ cubic-phase ZrW_2O_8 . The DFT-calculated lattice constant with Perdew-Burke-Ernzerhof solid (PBEsol) is 9.215 Å, slightly larger than 9.160 Å in experiment [10]. In the first iteration of DP-GEN workflow, the configurations of the initial training dataset contain 200 randomly perturbed structures of 44-atom cubic cell. The maximum magnitude of perturbed displacement for atomic coordinates is 0.01 Å, and the strain is -0.003 to 0.003 of the ground-state lattice parameters. Starting with the above training datasets, four different DPs are trained using the DeepMD method [26,27], based on different values of deep neural network parameters. The exploration step was performed in which one of the DPs is used for MD simulations at given pressure and temperature to explore the configuration space. For all sampled configurations in MD trajectories, the other three DPs will predict the atomic forces of all atoms. The maximum deviation of the four DP-predicted forces (σ_f^{\max}) can be used to formulate the criterion for labeling configurations:

$$\sigma_f^{\max} = \max \sqrt{\langle |F_i - \langle F_i \rangle|^2 \rangle},$$

where $\langle \dots \rangle$ indicates the average of DP-predicted force, and F_i denotes the predicted force on the atom i . The explored configurations possess the characteristic of $\sigma_f^{\max} < \sigma_{\text{low}}$, indicating they are already well described with a high accuracy by the current DP, which is labeled as accuracy, whereas an explored configuration with $\sigma_f^{\max} > \sigma_{\text{high}}$ is highly distorted and unphysical due to poor model quality of DP and is thus labeled as failure. The failure ratio is often high in the first several iterations. Only configurations satisfying $\sigma_{\text{low}} < \sigma_f^{\max} < \sigma_{\text{high}}$ are selected as candidates for further self-consistent DFT calculation and are added to the training dataset for training in the next iteration. The σ_f^{\max} can be also used as the convergence criterion for DP-GEN iterations, and the DP-GEN iterations are considered converged when the accuracy ratio is larger than 99%. Here, the σ_{low} and σ_{high} are set to 0.05 and 0.15 eV/Å in the iterations for 50 to 550 K, and 0.08 and 0.25 eV/Å in the iterations for 600 to 1500 K to ensure the convergence. Finally, by iterating above procedure 56 times, 20 460 configurations were obtained for training. For more details of the DP-GEN process, please refer to the original literature or our previous work of developing SrTiO₃ DP [32,42].

B. DP-GEN iteration process and generation of the training dataset

To obtain the training dataset, we perform the DP-GEN iteration process. The distributions of σ_f^{\max} for different temperatures in the first five iterations are shown in Fig. S18 [41], and the detailed ratios of the accurate, candidate, and failed configurations in the first 15 iterations are shown in Table SII. In the first iteration, starting with $P2_13$ cubic phase, the majority of the configurations were labeled either as candidate (22.05%) or failed (73.15%), because the incipient DP is rough due to the confined configuration space. After adding a few thousand candidate configurations into the training dataset in latter iterations and a complete training, all sampled low-temperature configurations (50–200 K) were labeled as accurate. To explore a wider configuration space, high-temperature configurations (200–1400 K) from finite-

temperature DPMD simulations are added at later exploration steps. The whole DP-GEN iteration process starts with 150 initial perturbed cubic configurations, then proceeds to explore 1×10^7 configurations. Finally, the σ_f^{\max} convergence to 99.7% and only 20 460 candidate configurations were selected for labeling and added into the training dataset after 56 DP-GEN iterations. All exploration settings and calculation files are available in DP-library website [54].

C. Training the DP

The DEEPM-D-KIT code is used for training of DP [55]. In the deep neural network of DP, the total potential energy of a configuration is assumed to be a sum of each atomic energy, which is mapped from a descriptor through an embedding network. The descriptor characterizes the local environment of atom within a cutoff radius R_c . Here, the R_c is set to 6 Å. The maximum number of atoms within the R_c is set to 50 for Zr, 100 for W, and 400 for O, respectively. The translational, rotational, and permutational symmetry of the descriptor are preserved by another embedding network. The smooth edition of the DP model was employed to remove the discontinuity introduced by the R_c [27]. The sizes of the embedding and fitting networks are (25, 50, 100) and (240, 240, 240), respectively. The loss function used in this work has the same form as our recent work [32]. The weight coefficients of the energy, atomic force, and virial terms in the loss functions change during the optimization process from 0.2 to 1, 500 to 1, and 0.02 to 0.2. The DPs are trained with 1 800 000 steps by learning rate decaying from 1×10^{-3} to 3.5×10^{-8} exponentially. The model compression scheme was applied in this work for boosting the computational efficiency of the DPMD simulation [56].

D. DFT calculations

The initial training dataset in the first iteration is obtained by performing a ten-step *ab initio* molecular-dynamics (MD) simulation for randomly perturbed 44 atoms cubic cell at 50 K. After labeling candidate configurations, self-consistent DFT calculations were performed subsequently. The DFT calculations were performed using a plane-wave basis set with a cutoff energy of 500 eV as implemented in the Vienna *Ab initio* Simulation Package (VASP) [57,58], and the electron exchange-correlation potential was described using the generalized gradient approximation and PBEsol scheme [59]. The Brillouin zone was sampled with a $4 \times 4 \times 4$ Monkhorst-Pack k -point grid for the cubic unit cell.

E. Molecular dynamics simulations

In exploration step, the MD simulations were performed using LAMMPS code with periodic boundary conditions [60]. The MD simulations adopt the isobaric-isothermal (NPT) ensemble with temperature set from 10 to 1500 K and pressure set from 1 bar to 5 GPa, because the explorative temperature and pressure should be large than the ones for subsequent NTE and PIA simulations. A Nosé-Hoover thermostat and Parrinello-Rahman barostat are employed to control temperature and pressure, respectively [61,62]. The time step in simulations is set to 1 fs.

The optimized DP can be used to study the atomic dynamics driven by temperature and pressure via performing deep-potential MD simulations. The DPMD simulations starting with $8 \times 8 \times 8$ supercell (i.e., $7.3 \text{ nm} \times 7.3 \text{ nm} \times 7.3 \text{ nm}$) of optimized cubic α -ZrW₂O₈ phase containing 22 528 atoms. All results about NTE and PIA of ZrW₂O₈ were executed by DPMD simulations. For NTE simulations, the equilibrium run is 50 ps, followed by a production run of 100 ps at a specified temperature. The lattice constant, true/apparent bond length (angle) were calculated by the average of 200 snapshots in 100 ps of equilibrium state. For PIA simulations, cubic symmetry was imposed (isotropic changes in cell lengths) during NPT simulations. The “lattice constants” of pressure-induced amorphous phase are defined as $\sqrt[3]{V}/8$, where V is the volume of the simulated $8 \times 8 \times 8$ supercell. The simulation times for compression and decompression were set to 50 and 100 ps, respectively. To prove the stability of retained a^{III} amorphous phase, we lengthen the decompression time to 2 ns, and found the a^{III} amorphous phase is maintained (Supplemental Material, Fig. S11 [41]). We also lengthen the compression

time to prove the second critical pressure of 3.8 GPa slightly depends on compression time (Supplemental Material, Fig. S12 [41]).

ACKNOWLEDGMENTS

This paper was supported by the National Key R&D Program of China (Grant No. 2021YFA0718900), the Key Research Program of Frontier Sciences of CAS (Grant No. ZDBS-LY-SLH008), the National Nature Science Foundation of China (Grant No. 11974365), and the K.C. Wong Education Foundation (Grant No. GJTD-2020-11).

All the input files, final training datasets, and DP model files to reproduce the results contained in this paper are available in DP-library website [54].

The DFT calculations, MD simulations, concurrent learning procedure, and deep neural network training were performed with VASP, LAMMPS, DP-GEN, and DEEPM-D-KIT code. The latter three are open-source codes available at and [65a,65b].

-
- [1] M. T. Dove, *Structure and Dynamics: An Atomic View of Materials* (Oxford University Press, Oxford, UK, 2003).
- [2] C. A. Perottoni and J. A. H. da Jornada, *Science* **280**, 886 (1998).
- [3] G. D. Barrera, J. A. O. Bruno, T. H. K. Barron, and N. L. Allan, *J. Phys.: Condens. Matter* **17**, R217 (2005).
- [4] W. Miller, C. Smith, D. Mackenzie, and K. Evans, *J. Mater. Sci.* **44**, 5441 (2009).
- [5] P. H. Poole, F. Sciortino, U. Essmann, and H. E. Stanley, *Nature (London)* **360**, 324 (1992).
- [6] O. Mishima and H. E. Stanley, *Nature (London)* **392**, 164 (1998).
- [7] S. Woutersen, B. Ensing, M. Hilbers, Z. Zhao, and C. A. Angell, *Science* **359**, 1127 (2018).
- [8] A. P. Drozdov, M. I. Erements, I. A. Troyan, V. Ksenofontov, and S. I. Shylin, *Nature (London)* **525**, 73 (2015).
- [9] A. P. Drozdov, P. P. Kong, V. S. Minkov, S. P. Besedin, M. A. Kuzovnikov, S. Mozaffari, L. Balicas, F. F. Balakirev, D. E. Graf, V. B. Prakapenka *et al.*, *Nature (London)* **569**, 528 (2019).
- [10] T. A. Mary, J. S. O. Evans, T. Vogt, and A. W. Sleight, *Science* **272**, 90 (1996).
- [11] D. Cao, F. Bridges, G. R. Kowach, and A. P. Ramirez, *Phys. Rev. Lett.* **89**, 215902 (2002).
- [12] D. Cao, F. Bridges, G. R. Kowach, and A. P. Ramirez, *Phys. Rev. B* **68**, 014303 (2003).
- [13] A. Sanson, *Chem. Mater.* **26**, 3716 (2014).
- [14] A. K. A. Pryde, K. D. Hammonds, M. T. Dove, V. Heine, J. D. Gale, and M. C. Warren, *J. Phys.: Condens. Matter* **8**, 10973 (1996).
- [15] A. K. Pryde, K. D. Hammonds, M. T. Dove, V. Heine, J. D. Gale, and M. C. Warren, *Phase Transitions* **61**, 141 (1997).
- [16] M. G. Tucker, A. L. Goodwin, M. T. Dove, D. A. Keen, S. A. Wells, and J. S. O. Evans, *Phys. Rev. Lett.* **95**, 255501 (2005).
- [17] M. T. Dove and H. Fang, *Rep. Prog. Phys.* **79**, 066503 (2016).
- [18] T. R. Ravindran, A. K. Arora, and T. A. Mary, *Phys. Rev. Lett.* **84**, 3879 (2000).
- [19] J. S. O. Evans, Z. Hu, J. D. Jorgensen, D. N. Argyriou, S. Short, and A. W. Sleight, *Science* **275**, 61 (1997).
- [20] R. J. Speedy, *J. Phys.: Condens. Matter* **8**, 10907 (1996).
- [21] T. Varga, A. P. Wilkinson, A. C. Jupe, C. Lind, W. A. Bassett, and C.-S. Zha, *Phys. Rev. B* **72**, 024117 (2005).
- [22] A. K. Arora, V. S. Sastry, P. C. Sahu, and T. A. Mary, *J. Phys.: Condens. Matter* **16**, 1025 (2004).
- [23] D. A. Keen, A. L. Goodwin, M. G. Tucker, M. T. Dove, J. S. O. Evans, W. A. Crichton, and M. Brunelli, *Phys. Rev. Lett.* **98**, 225501 (2007).
- [24] C. A. Figueiredo, J. Catafesta, J. E. Zorzi, L. Salvador, I. J. R. Baumvol, M. R. Gallas, J. A. H. da Jornada, and C. A. Perottoni, *Phys. Rev. B* **76**, 184201 (2007).
- [25] C. Pantea, A. Migliori, P. B. Littlewood, Y. Zhao, H. Ledbetter, J. C. Lashley, T. Kimura, J. Van Duijn, and G. R. Kowach, *Phys. Rev. B* **73**, 214118 (2006).
- [26] L. Zhang, J. Han, H. Wang, R. Car, and W. E., *Phys. Rev. Lett.* **120**, 143001 (2018).
- [27] L. Zhang, J. Han, H. Wang, W. A. Saidi, R. Car, and E. Weinan, End-to-end symmetry preserving inter-atomic potential energy model for finite and extended systems, in *Proceedings of the 32nd International Conference on Neural Information Processing Systems, NIPS'18* (Curran Associates, Inc., Red Hook, NY, 2018), pp. 4441–4451.
- [28] H. Fang, M. T. Dove, L. H. N. Rimmer, and A. J. Misquitta, *Phys. Rev. B* **88**, 104306 (2013).
- [29] T. Wen, L. Zhang, H. Wang, W. E., and D. J. Srolovitz, *Mater. Futures* **1**, 022601 (2022).
- [30] V. L. Deringer, N. Bernstein, G. Csányi, C. Ben Mahmoud, M. Ceriotti, M. Wilson, D. A. Drabold, and S. R. Elliott, *Nature (London)* **589**, 59 (2021).
- [31] L. Zhang, H. Wang, R. Car, and W. E., *Phys. Rev. Lett.* **126**, 236001 (2021).

- [32] R. He, H. Wu, L. Zhang, X. Wang, F. Fu, S. Liu, and Z. Zhong, *Phys. Rev. B* **105**, 064104 (2022).
- [33] H. Niu, L. Bonati, P. M. Piaggi, and M. Parrinello, *Nat. Commun.* **11**, 2654 (2020).
- [34] M. F. Calegari Andrade, H.-Y. Ko, L. Zhang, R. Car, and A. Selloni, *Chem. Sci.* **11**, 2335 (2020).
- [35] J. Zeng, L. Cao, M. Xu, T. Zhu, and J. Z. H. Zhang, *Nat. Commun.* **11**, 5713 (2020).
- [36] H. Nakata, M. Filatov, and C. H. Choi, *ACS Appl. Mater. Interfaces* **14**, 26116 (2022).
- [37] Z. Wei, L. Tan, G. Cai, A. E. Phillips, I. da Silva, M. G. Kibble, and M. T. Dove, *Phys. Rev. Lett.* **124**, 255502 (2020).
- [38] R. Ma, Z. Liu, Y. Cao, Q. Li, K. Lin, K. Ohara, X. Chen, L. Chen, H. Xu, J. Deng *et al.*, *Inorg. Chem.* **61**, 8634 (2022).
- [39] X. Zhang, X. Jiang, M. S. Molokeev, N. Wang, Y. Liu, and Z. Lin, *Chem. Mater.* **34**, 4195 (2022).
- [40] S. Liu, M.-Q. Long, and Y.-P. Wang, *Appl. Phys. Lett.* **120**, 072403 (2022).
- [41] See Supplemental Material at <http://link.aps.org/supplemental/10.1103/PhysRevB.106.174101> for discussion of γ phase, Tables SI, SII, and Figs. S1–S18; also see Refs. [19,24,25,63,64].
- [42] Y. Zhang, H. Wang, W. Chen, J. Zeng, L. Zhang, H. Wang, and W. E, *Comput. Phys. Commun.* **253**, 107206 (2020).
- [43] J. A. Greathouse, P. F. Weck, M. E. Gordon, E. Kim, and C. R. Bryan, *J. Phys.: Condens. Matter* **32**, 085401 (2019).
- [44] J. Li, S. Meng, L. Qin, and H. Lu, *Solid State Commun.* **247**, 58 (2016).
- [45] N. Duan, U. Kameswari, and A. W. Sleight, *J. Am. Chem. Soc.* **121**, 10432 (1999).
- [46] H. Fang, M. T. Dove, and K. Refson, *Phys. Rev. B* **90**, 054302 (2014).
- [47] A. V. Tkachenko and I. A. Zaloznyak, *Phys. Rev. B* **103**, 134106 (2021).
- [48] J. Catafesta, J. E. Zorzi, C. A. Perottoni, M. R. Gallas, and J. A. H. Da Jornada, *J. Am. Ceram. Soc.* **89**, 2341 (2006).
- [49] O. B. Tsiok, V. V. Brazhkin, A. G. Lyapin, and L. G. Khvostantsev, *Phys. Rev. Lett.* **80**, 999 (1998).
- [50] K. W. Chapman and P. J. Chupas, *J. Am. Chem. Soc.* **129**, 10090 (2007).
- [51] H. Fang, M. T. Dove, and A. E. Phillips, *Phys. Rev. B* **89**, 214103 (2014).
- [52] H. Fang and M. T. Dove, *Phys. Rev. B* **87**, 214109 (2013).
- [53] H. Fang and M. T. Dove, *J. Phys: Condens. Matter* **26**, 115402 (2014).
- [54] <https://dplibrary.deepmd.net/>.
- [55] H. Wang, L. Zhang, J. Han, and W. E, *Comput. Phys. Commun.* **228**, 178 (2018).
- [56] D. Lu, W. Jiang, Y. Chen, L. Zhang, W. Jia, H. Wang, and M. Chen, *J. Chem. Theory Comput.* **18**, 5559 (2022).
- [57] G. Kresse and J. Furthmüller, *Phys. Rev. B* **54**, 11169 (1996).
- [58] G. Kresse and J. Furthmüller, *Comput. Mater. Sci.* **6**, 15 (1996).
- [59] J. P. Perdew, K. Burke, and M. Ernzerhof, *Phys. Rev. Lett.* **78**, 1396 (1997).
- [60] S. Plimpton, *J. Comput. Phys.* **117**, 1 (1995).
- [61] S. Nosé, *J. Chem. Phys.* **81**, 511 (1984).
- [62] T. Riste, E. J. Samuelsen, K. Otnes, and J. Feder, *Solid State Commun.* **9**, 1455 (1971).
- [63] J. S. O. Evans, J. D. Jorgensen, S. Short, W. I. F. David, R. M. Ibberson, and A. W. Sleight, *Phys. Rev. B* **60**, 14643 (1999).
- [64] J. S. Evans, W. David, and A. Sleight, *Acta Crystallogr., Sect. B: Struct. Sci* **55**, 333 (1999).
- [65] The DFT calculations, MD simulations, concurrent learning procedure, and deep neural network training were performed with VASP, LAMMPS, DP-GEN, and DEEPM-D-KIT code. The latter three are open-source codes available at <https://lammps.sandia.gov> and <https://github.com/deepmodeling>.